IOP Publishing J. Phys. Mater. **6** (2023) 034003 https://doi.org/10.1088/2515-7639/acce6f

Journal of Physics: Materials

OPEN ACCESS

RECEIVED
22 December 2022

REVISED
7 April 2023

ACCEPTED FOR PUBLICATION
19 April 2023

PUBLISHED
10 May 2023

PAPER

Magnetic-field-controlled growth of magnetoelastic phase domains in FeRh

Jon Ander Arregi[1,*], **Friederike Ringe**[1], **Jan Hajduček**[1], **Olena Gomonay**[2], **Tomáš Molnár**[1,3], **Jiří Jaskowiec**[1] and **Vojtěch Uhlíř**[1,3]

[1] CEITEC BUT, Brno University of Technology, Purkyňova 123, 612 00 Brno, Czech Republic
[2] Institute of Physics, Johannes Gutenberg-University Mainz, Staudingerweg 7, 55099 Mainz, Germany
[3] Institute of Physical Engineering, Brno University of Technology, Technická 2, 616 69 Brno, Czech Republic
[*] Author to whom any correspondence should be addressed.

E-mail: ja.arregi@ceitec.vutbr.cz

Keywords: first-order phase transition, FeRh, magnetic phase domains, magnetostriction, optical microscopy

Abstract

Magnetic phase transition materials are relevant building blocks for developing green technologies such as magnetocaloric devices for solid-state refrigeration. Their integration into applications requires a good understanding and controllability of their properties at the micro- and nanoscale. Here, we present an optical microscopy study of the phase domains in FeRh across its antiferromagnetic–ferromagnetic phase transition. By tracking the phase-dependent optical reflectivity, we establish that phase domains have typical sizes of a few microns for relatively thick epitaxial films (200 nm), thus enabling visualization of domain nucleation, growth, and percolation processes in great detail. Phase domain growth preferentially occurs along the principal crystallographic axes of FeRh, which is a consequence of the elastic adaptation to both the substrate-induced stress and laterally heterogeneous strain distributions arising from the different unit cell volumes of the two coexisting phases. Furthermore, we demonstrate a magnetic-field-controlled directional growth of phase domains during both heating and cooling, which is predominantly linked to the local effect of magnetic dipolar fields created by the alignment of magnetic moments in the emerging (disappearing) FM phase fraction during heating (cooling). These findings highlight the importance of the magnetoelastic character of phase domains for enabling the local control of micro- and nanoscale phase separation patterns using magnetic fields or elastic stresses.

1. Introduction

Understanding magnetic phase transition materials at the micro- and nanoscale is a key for technologically exploiting their phase-change functionalities linked to the variations of order parameters in response to an external driving force [1, 2]. Interconnection among order parameters in first-order phase transitions typically leads to complex behavior of phase separated states that is highly dependent on both intrinsic (e.g. crystal symmetry, magnetic exchange interactions) and extrinsic factors (e.g. substrate-induced strain, defects, disorder) [3–5]. These ingredients provide rich opportunities for making designer materials for applications in energy conversion [6], magnetoelastic actuation [7], and low-power devices [8].

In this work, we focus on the FeRh alloy, which undergoes a magnetostructural phase transition from antiferromagnetic (AF) to ferromagnetic (FM) order when heated above 360 K [9]. The AF-to-FM phase transition in FeRh only exists near the equiatomic composition [10], with the change in magnetic order being accompanied by an isotropic lattice expansion ($\sim$0.6%) [11] and a $\sim$50% reduction in resistivity [12–14]. The transition is first-order in nature, possessing a hysteresis of $\sim$10–20 K between the heating and cooling cycles [15]. In conjunction with the large changes in magnetization, lattice parameter, and resistivity, the phase transition displays a large entropy variation [16, 17]. Among first-order phase transition materials, magnetocaloric effects seem to be particularly pronounced in FeRh [18–20], for which the highest values of adiabatic temperature change were reported for applied field variations up to 2 T [17, 21, 22]. The option to control the phase transition using electric fields via piezoelectric substrates [23–26] also makes this material interesting for exploring electro-magnetocaloric effects.

As the system progresses through the first-order phase transition, latent heat is absorbed (released) during heating (cooling) [27], causing phase separation at the micro- and nanoscale. Imaging techniques capable of following temperature-dependent variations of order parameters yield valuable information about the heterogeneous nature of the magnetostructural transition in real space, provided that they can resolve the characteristic size of AF/FM regions.

Early reports using magnetic force microscopy (MFM) confirmed phase coexistence in FeRh by tracking the magnetic stray field from sub-micron FM regions [28, 29]. In the last decade, the temperature-dependent evolution of FM domains has been analyzed in detail for high-quality epitaxial films by using x-ray magnetic circular dichroism in photoemission electron microscopy (XMCD-PEEM) [30–32], together with its x-ray magnetic linear dichroism counterpart, XMLD-PEEM, additionally enabling to distinguish the spin axis of AF domains [33]. Despite the limited probing depth of ∼5 nm, these measurements achieved establishing the typical size of laterally separated AF/FM regions between 0.1–1 µm, and clearly identified mechanisms such as domain nucleation, growth, and coalescence [30].

Furthermore, x-ray nanodiffraction experiments confirmed the sub-micron character of structural phase domains in FeRh [34, 35]. FM domain evolution across the phase transition was also studied in real space with complementary techniques that are sensitive to magnetization, such as scanning electron microscopy with polarization analysis [36], electron holography and differential phase contrast in transmission electron microscopy [37, 38], or nitrogen-vacancy-center magnetometry [39].

Alternatively, it is possible to exploit the electronic character of the phase transition and the associated change in the optical refractive index, as in the metallic and insulating phases of VO_2 [40] or martensitic twin variants in Ni_2MnGa [41–43]. Optical measurements provide a fast and versatile way to observe the underlying key physical mechanisms within first-order phase transitions, such as metallic filament growth processes in insulator-to-metal transitions [44].

For FeRh, a ∼5% decrease of the optical reflectivity was reported in the red and infrared spectral region upon the AF-to-FM phase transition [45]. Scanning focused-laser measurements allow visualizing the distribution of phase domains in thin films by tracking the space-resolved reflectivity [45]. Recently, wide-field optical microscopy was utilized to distinguish FM-stabilized ion beam irradiated areas in the AF FeRh film matrix [46], or to distinguish bcc-like and fcc-like ordered FeRh grains in bulk samples based on whether they exhibit or lack a decrease in optical reflectivity upon heating, respectively [47]. However, mesoscale nucleation and growth processes of AF/FM domains in FeRh have not been studied in detail using optical microscopy, which is partially limited by the characteristic phase domain size being below the optical resolution limit [30].

In this paper, we employ wide-field optical microscopy to track the evolution of phase domains in an epitaxial FeRh film. It is found that the dimensions of phase separated regions are on the micron scale, which enables optical imaging of domain nucleation, growth, and percolation processes during the thermally-driven transition. Imaging the distribution of AF and FM domains across the thermally driven phase transition allows identifying the domains' shape and orientation, which are determined by the domains' elastic adaptation to the substrate and to lateral strain arising from the heterogeneous nature of AF/FM phase coexistence. Finally, we demonstrate that applying a sufficiently large magnetic field causes a selective directional growth of the product phase along the field direction during both heating and cooling cycles. We discuss our results in terms of the interplay of the magnetic and elastic degrees of freedom, highlighting the relevance of the magnetoelastic character of phase domains in FeRh.

2. Methods

FeRh films were epitaxially grown onto single-crystal MgO(001) substrates using magnetron sputtering from an equiatomic FeRh target. The substrates were initially preheated to 700 K in high vacuum for 1 h to reconstruct their surface. FeRh growth was performed at the same temperature, using an argon pressure of 2.7×10^{-3} mbar and a sputter power of 50 W, resulting in a deposition rate of 2 nm min^{-1}. The films were post-growth annealed at 1050 K for 80 min to improve their chemical ordering and to obtain the desired B2 (CsCl-type) structure. Samples were capped with a 2 nm-thick Pt layer after cooling down below 400 K.

Magnetization measurements were performed via vibrating sample magnetometry (VSM) using a Quantum Design Versalab magnetometer. Temperature-dependent magnetization data are presented after subtracting the diamagnetic substrate contribution.

The crystallographic structure of the films was analyzed via x-ray diffraction (XRD) employing a Rigaku Smartlab 9 kW diffractometer with monochromated Cu–K_α radiation ($\lambda = 1.5406$ Å). Additionally, high-resolution transmission electron microscopy (HRTEM) and selected area electron diffraction (SAED) analysis were performed using an image-corrected FEI Titan Themis 60-300 Cubed working at 300 kV. Electron transparent cross-section lamellae for TEM analysis were fabricated using a dual-beam system FEI Helios NanoLab 660 with a Ga liquid metal ion source type focused ion beam (FIB). The sample stoichiometry of cross section lamellae was verified using energy dispersive x-ray spectroscopy (EDX) using an FEI SUPER-X spectrometer in scanning TEM (STEM) mode. Diffraction patterns were acquired in the SAED mode with a 10 µm-diameter selected area aperture, corresponding to an imaging region of ∼200 nm in diameter in the specimen plane.

Phase domain visualization and magneto-optical characterization were carried out using a high-resolution optical microscope from Evico magnetics with 50× or 100× magnification objective lenses. A rotatable electromagnet provides applied magnetic fields up to 400 mT in the plane of the sample. The sample temperature is controlled between 290 and 410 K at ambient conditions using a custom-made sample holder based on a dual-stage Peltier cell.

Atomic force microscopy (AFM) and MFM measurements were acquired using a Dimension Icon microscope (Bruker Corp.) with CoCr coated MESP probes. MFM images are acquired in a constant external magnetic field of ∼300 mT produced by a permanent magnet and oriented perpendicular to the sample plane. A different custom-made sample holder based on two Peltier modules allows temperature regulation up to 380 K at ambient conditions. AFM/MFM data were analyzed and visualized using the open-source *Gwyddion* software [48].

Calculations of elastic strain distributions for coexisting phase domains were performed based on the standard theory of elasticity and using the Partial Differential Equation Toolbox of MATLAB. We considered an effective 2D model with isotropic elasticity and typical values of elastic coefficients for both AF and FM phases (a Poisson's ratio value of 0.3 and a Young's modulus amounting to 90 GPa), and assumed a 0.1% in-plane expansion upon the AF-to-FM transition [11].

3. Results

3.1. FeRh film characterization

The sample under investigation consists of a 200 nm-thick epitaxial FeRh film on an MgO(001) substrate. Figure 1(a) shows the evolution of the sample's magnetization, as measured via VSM, demonstrating the thermally induced phase transition above room temperature. The sample shows a prominent appearance of magnetization above ∼364 K during heating, with a comparable drop in magnetization at ∼357 K during cooling. The residual FM moment at room temperature amounts to ∼4% of magnetization in the high-temperature FM phase.

Room-temperature XRD characterization in figure 1(b) demonstrates the attainment of the B2 crystal structure and the FeRh(001)/MgO(001) out-of-plane crystallographic orientation. The FeRh lattice epitaxially adapts to the MgO structure by introducing a 45° rotation between the principal axes of the two lattices (i.e. FeRh[100] || MgO[110]) [11, 15]. Figure 1(c) exhibits a TEM micrograph of the cross-section lamella of an FeRh thin film, showing a sharp interface between FeRh and MgO. The ion-beam-induced carbon capping layer used for FIB lamella fabrication is visible on top of the FeRh film. The inset in figure 1(c) displays an HRTEM image of the FeRh/MgO interface region.

Additional analysis of the FeRh film structure is performed using SAED in two electron transparent lamellae for TEM observation along the MgO[100] and MgO[110] zone axes (figures 1(d) and (e)). The diffraction pattern is taken in both cases from a ∼200 nm-diameter region close to the FeRh/MgO interface. The patterns show well defined diffraction spots corresponding to the MgO and FeRh lattices (see main diffraction spots labeled in figures 1(d) and (e)). SAED patterns confirm the predominant presence of the B2 phase of FeRh, 45° in-plane rotated with respect to the MgO lattice. Furthermore, STEM–EDX mapping of the FeRh film confirms the one-to-one Fe:Rh stoichiometry across the whole thickness. Additional faint reflections are present in both SAED patterns (figures 1(d) and (e)), indicating a minor presence of other crystalline FeRh phases and/or orientations. These were previously interpreted as a signature of fcc-like FeRh phase in the predominant bcc-like B2 phase matrix [49–51], typically located at the FeRh/MgO interface even in high-quality epitaxial films [51]. Lattice distortions and a minor presence of fcc-like phase could also

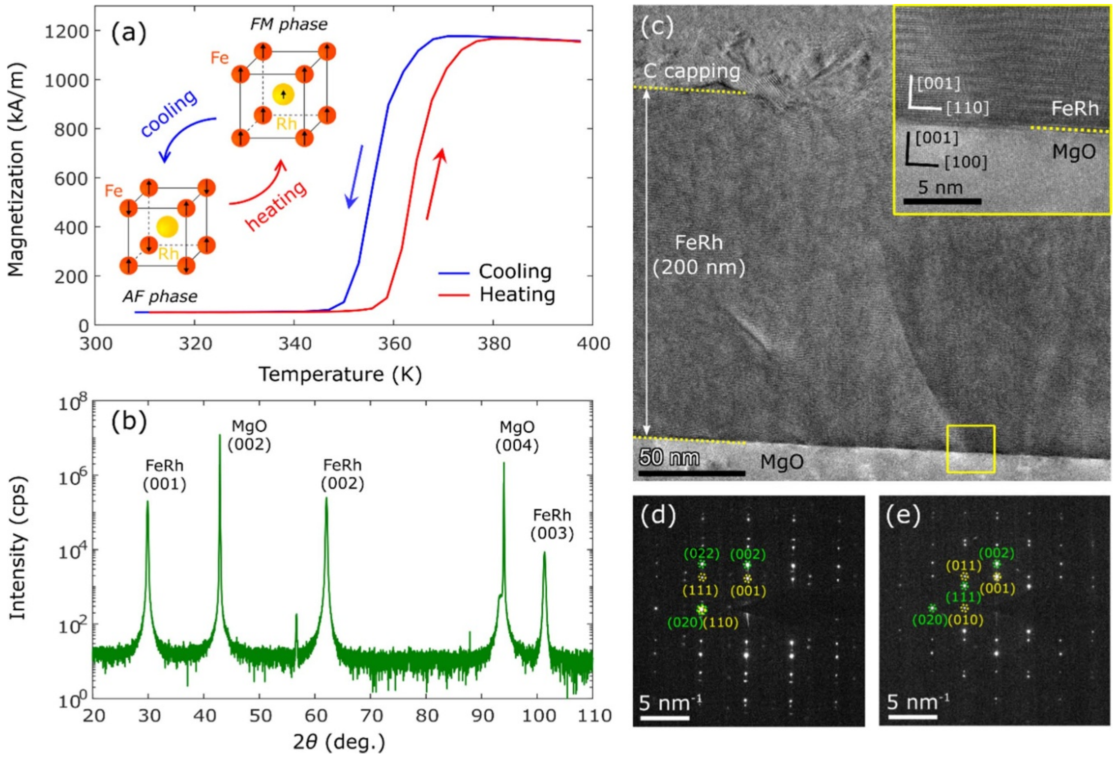

Figure 1. Magnetic and structural properties of a 200 nm-thick FeRh film on MgO(001). (a) Temperature-dependent magnetization data measured for an in-plane field of 1 T along the FeRh[110] direction. The red and blue arrows indicate the heating and cooling cycles, respectively. The magnetization data were corrected by 8 K in temperature to account for the field-induced shift of the phase transition temperature [15]. The inset in (a) shows a schematic of the FeRh unit lattice to illustrate the associated modifications upon the phase transition. (b) Symmetric XRD θ–2θ scan measured at room temperature indicating the FeRh(001) out-of-plane texture of the film and the attainment of the B2 crystal structure in FeRh. (c) TEM micrograph of a cross-section lamella of the analyzed film. The inset in the yellow square shows a HRTEM image of the FeRh/MgO interface. SAED patterns of the interface region along the (d) MgO[100] and (e) MgO[110] zone axis. The diffraction spots indicated in yellow and green color correspond to FeRh and MgO, respectively.

explain the presence of moiré fringes in the HRTEM image in the inset of figure 1(c) [50]. The net amount of the fcc-like crystalline phase across the full FeRh film is not significant, as concluded from the absence of fcc-like reflections in the XRD scan shown in figure 1(b).

3.2. Nucleation and growth of phase domains in zero field

The space-resolved optical reflectivity of the 200 nm-thick FeRh sample is firstly monitored at zero applied magnetic field using wide-field optical microscopy. Figures 2(a) and (b) exhibit a sequence of optical images with a field of view of 40 × 30 μm^2 during the heating and cooling cycles, respectively. The displayed snapshots are referenced with respect to the room temperature state (AF state) via subtraction. In the images, the horizontal direction corresponds to the in-plane MgO[100] substrate direction, with the FeRh[100] axis pointing along the diagonal (see the inset in the first snapshot of figure 2(a)).

As the sample is warmed up across the phase transition (figure 2(a)), we observe nucleation of FM regions, denoted by the local darker contrast arising from the drop in reflectivity upon the AF-to-FM transformation [45]. The nucleated FM regions typically appear as rectangular clusters of ∼1–2 μm in length upon their emergence, but quickly elongate along one of the diagonals in the image (corresponding to the principal in-plane crystallographic axes of FeRh, [100] and [010]) upon further increasing the temperature. As the FM phase progresses, it becomes clear that FM regions grow in a zig-zag fashion following the diagonal directions of the image. The growing FM domains initially avoid percolation, forming a 45°-rotated, rectangular tessellation network within the remaining matrix of the parent AF phase. As temperature is further increased, FM domains eventually coalesce (figure 2(a)).

We also notice that the onset of the phase transition is delayed around topographical hole-like defects during heating (see the two irregular spots in figure 2(a)). The FM phase nucleates and grows last around these defects as temperature increases, while the same spots act as nucleation centers for the AF phase during cooling (figure 2(b)). The FM-to-AF phase transition proceeds in an equivalent way to the one during heating, except for the fact that AF regions seem to grow very quickly from the defects acting as nucleation centers, forming better connected AF networks in the FM parent matrix. AF domain growth occurs in the

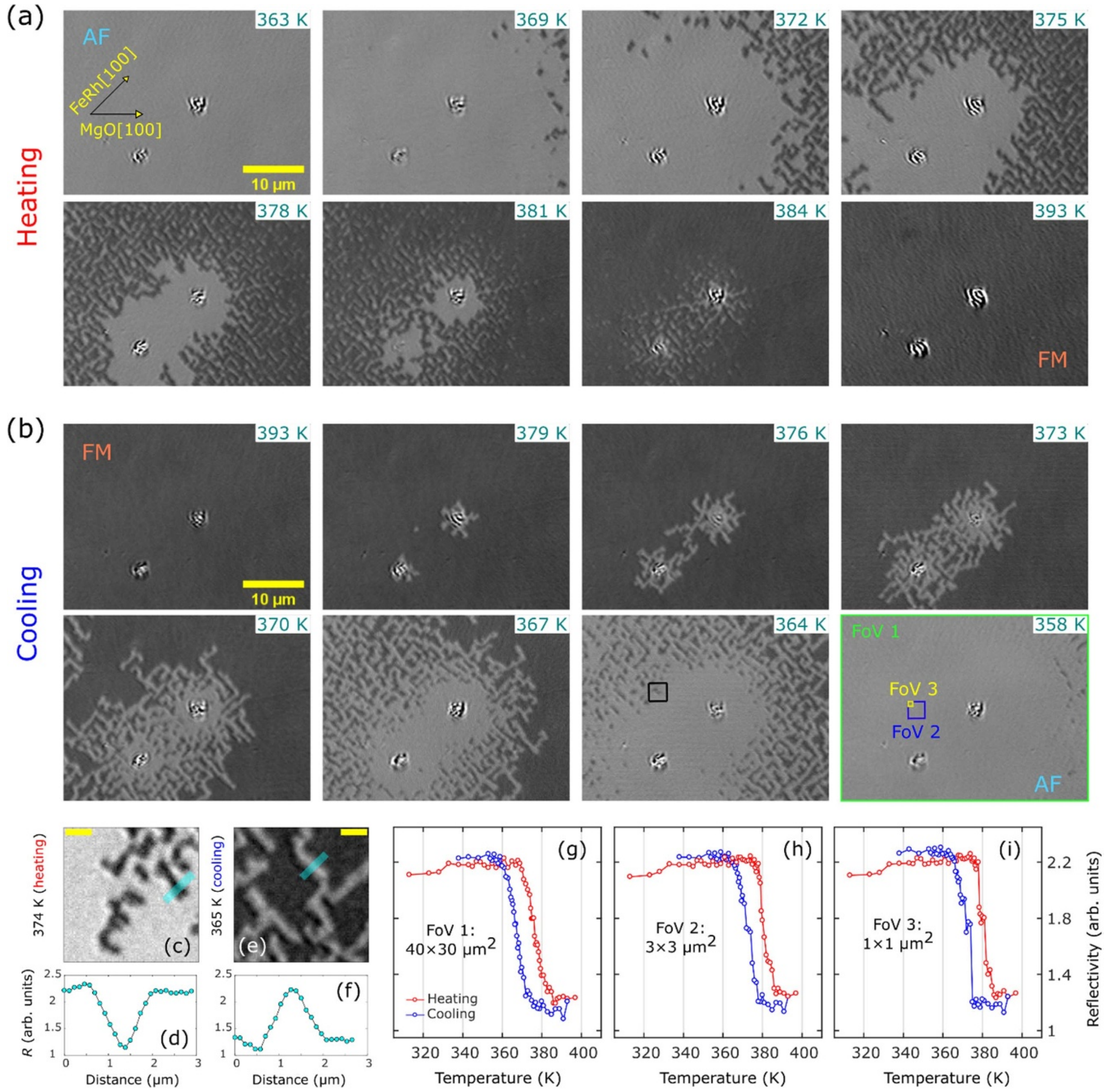

Figure 2. Optical imaging of the magnetostructural phase transition in FeRh at zero applied magnetic field. Snapshots of optical reflectivity images are shown over a 40 × 30 μm^2 area as the sample undergoes the phase transition during (a) heating and (b) cooling. The measurement temperature is indicated in the inset of each snapshot. AF (FM) regions are characterized by a brighter (darker) contrast due to the reflectivity drop upon the AF-to-FM phase transition. The inset in the first image in (a) shows the crystallographic orientations for FeRh and MgO. (c) Detail of FM domains in the AF matrix during heating (scale bar, 2 μm) and (d) line profile of optical reflectivity across an elongated FM domain. (e), (f) show the same information for AF domains in the FM matrix during cooling. (g)–(i) show the temperature dependence of optical reflectivity for different choices of the field-of-view (FoV), namely (g) FoV = 40 × 30 μm^2, (h) FoV = 3 × 3 μm^2, (i) FoV = 1 × 1 μm^2. The choices for FoV are indicated in the last image of (b).

same zig-zag fashion as during heating, showing predominant elongation along the main crystal axes of FeRh (diagonals in figure 2(b)). Growing AF domains also avoid coalescence at first, forming micron-sized L-shaped tessellations until percolation occurs at low enough temperatures.

Figure 2(c) shows a detail (10 × 10 μm^2) of FM domains in the AF matrix during cooling. A line scan of the optical reflectivity (figure 2(d)) reveals that the elongated FM domains have a short axis of 0.5–1 μm and a long axis of a few microns, enabling their observation by optical microscopy. The typical size of AF domains in the FM matrix during cooling is in the same range, as shown in figures 2(e) and (f).

We tracked the space-resolved reflectivity signal over a larger series of images (not shown here) using temperature steps of $\Delta T = 0.5$ K during the heating and cooling cycles. Figures 2(g)–(i) display the average optical reflectivity from regions with different sizes, namely 40 × 30 μm^2 (field of view in figures 2(a) and (b)), 3 × 3 μm^2 and 1 × 1 μm^2. The resulting curves exhibit well-defined thermal hysteresis curves even for the smallest considered region, allowing clear identification of the phase transition temperatures. As the size of the evaluated field of view reduces considerably, jumps in the optical reflectivity start to occur both in the heating and cooling cycles (figures 2(h) and (i)), recovering the abrupt nature of the first-order phase transition upon reducing the dimensions to the ∼1 μm^2 scale. The observed steps in reflectivity are

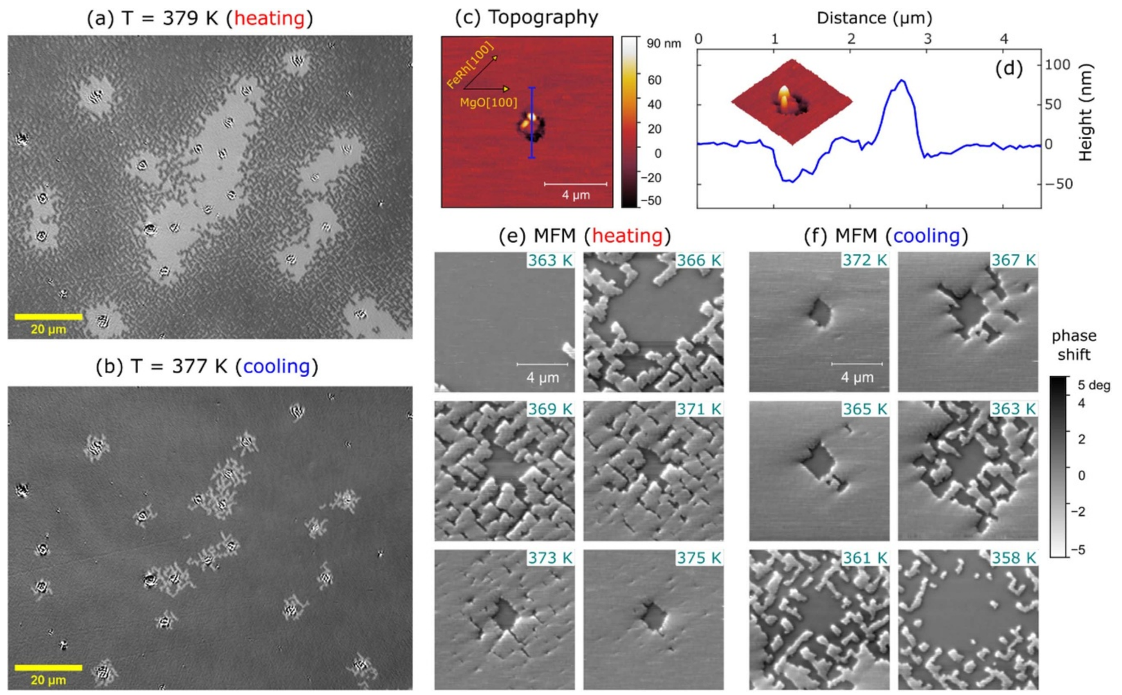

Figure 3. Character of the phase AF–FM transition in FeRh in the vicinity of topographic defects. The left panel shows optical microscopy images over 120 × 90 μm^2, exhibiting several topographic defects in the film. The images are taken (a) at the end of the AF-to-FM transition during heating and (b) at the beginning of the FM-to-AF transition during cooling. (c) AFM topography scan around a defect and (d) height profile along a line scan that vertically traverses the defect. The zero-value height in (c), (d) corresponds to the film surface. The inset shows a three-dimensional representation of the hole-like spot. MFM data measured around the defect during (e) heating and (f) cooling. Negative values of the MFM phase shift, represented by brighter areas, indicate FM regions, whereas darker areas correspond to AF regions with zero magnetic stray field.

consistently larger during cooling than heating, an observation that agrees well with the more prominent elongation of AF domains in the cooling cycle (figure 2(b)). A number of works on FeRh have already pointed out that this effect can be ascribed to the different kinetics of the transition during heating and cooling, where phase separation is more prominent in the latter [52], and can lead to remarkable supercooling behavior in nanoscale confined FeRh systems [13, 53].

We have further studied the topographic defects found at the surface of the FeRh film to determine their impact on the phase transition. Figures 3(a) and (b) display large-view optical images, where several topographic defects can be seen on the surface of the sample, with a lateral separation between defects of the order of ∼10 μm. AFM measurements at one of such topographic defects (figures 3(c) and (d)) reveal they consist of micron-sized grooves containing sub-micron hillocks that elevate above the film surface. We interpret the presence of these defects as solid-state dewetting centers that are formed during post-growth annealing of the samples. The film-to-substrate mismatch in surface energy and mass transport during annealing promote the formation of holes around impurities or stacking faults, leading to partial or advanced dewetting scenarios of the film [53, 54]. In our case, the grooves are about 50 nm deep (figure 3(d)) and do not reach all the way down to the substrate.

MFM measurements performed on the same topographic defect evidence that the FM phase appears the last around the groove, while the AF phase is first nucleated at the very edge of the groove (figures 3(e) and (f)). We explain this observation by arguing that compressive in-plane strain exerted by the MgO substrate on the film accumulates at the edges of the grooves in a complementary way to the situation where substrate-induced strain is relaxed at the edges of patterned mesoscale FeRh structures [32, 55]. This build-up of the in-plane compressive strain around holes promotes the AF phase over the FM one, significantly increasing the phase transition temperature in their vicinity. Hence the AF-to-FM transition during heating is delayed here, while the grooves provide an adequate nucleation site to initiate the reverse FM-to-AF phase transition during cooling. Optical microscopy imaging reveals such strain build-up around the grooves, which seems to extend laterally over a ∼10 μm scale (see figure 3(a)).

Next, we discuss the implications of elastic strain on the phase domain configuration during phase coexistence by examining the influence of the magnetic-phase-dependent unit cell volume in FeRh. It is generally considered that the expansion of the out-of-plane lattice parameter accommodates the majority of the ∼1% volume change upon the AF-to-FM phase transition. However, the in-plane lattice parameters of coexisting AF and FM regions in thin films can differ by ∼0.1%–0.15% (compared to ∼0.6% in the out-of-plane direction) at certain stages of the transition [11]. Thus, FeRh films need to adapt the existence of laterally heterogeneous strain distributions during phase separation.

We recall that phase domains in FeRh nucleate and grow forming a tessellated network of L-shaped AF/FM regions during both heating and cooling (see figures 2(a) and (b)). The characteristic lateral separation of phases is of the order of ∼1 µm, and percolation of large (>10 µm) homogeneous phase areas of the product phase only occurs in the final stages of the phase transition. We explain this in terms of the substrate-induced strain, which dictates that the films need to adapt the heterogeneous lateral strain distribution following the cubic, biaxial symmetry of the MgO substrate. This phenomenon is analogous to the substrate-strain-induced domain adaptation observed in epitaxial films with ferroelectric [56] or martensitic phases [41–43], where symmetry and the amount of lateral strain dictate the domain geometry.

In conjunction with the shape, the characteristic size of phase domains is greatly influenced by the epitaxial clamping of the film to the substrate. To illustrate this, let us assume that the AF FeRh lattice is fully relaxed and coincides with that of the MgO substrate. A nucleated FM cluster will tend to laterally expand upon its appearance due to the difference in specific energies of the AF and FM phases, but substrate clamping creates additional stresses in the cluster, limiting its expansion. The energy of the interface between the FM cluster and surrounding AF matrix also increases with the cluster size. The optimal size is then defined by the balance of all three factors.

For thinner epitaxial FeRh films, the substrate-induced stress becomes more relevant and de-stressing is introduced by alternating AF and FM domains at shorter intervals. We suggest that this is the reason behind the observation of small size phase domains ($\lesssim$500 nm) found so far in the literature for FeRh [30–36]. In our case, increasing the film thickness to 200 nm slightly reduces the relative weight of the elastic interaction coming from the substrate, allowing the formation of larger, micron-sized phase domains that can be visualized using optical microscopy.

The role of magnetoelastic coupling on the domain configuration of thin film AF systems has been recently highlighted in the literature. It is considered that deformations in the AF arising from spontaneous magnetoelasticity effects cause incompatibilities with the nonmagnetic substrate underneath, creating long-range destressing fields that establish the minimum energy magnetic domain configuration in the system [57–59]. Here, we follow a similar approach using the elasticity theory to examine the elastic incompatibility of the laterally adjacent and lattice mismatched AF/FM phases of FeRh during coexistence. We considered the spatial distribution of the laterally heterogeneous elastic fields around a FM (AF) cluster embedded in the AF (FM) film matrix during heating (cooling). We assumed a rectangular shape of the inclusion and considered different aspect ratio (AR) values. Despite the isotropic character of the spontaneous in-plane expansion $u_{xx}^{\mathrm{spon}} + u_{yy}^{\mathrm{spon}}$ associated with the AF–FM transition within the cluster (0.1%), the inclusion creates both isotropic ($u_{xx} + u_{yy}$) and anisotropic ($u_{xx} - u_{yy}$ and u_{xy}) strains in the AF matrix. The absolute value of anisotropic strains and the corresponding contribution to the energy of the sample depend on the AR. Figure 4(a) shows calculated $u_{xx} - u_{yy}$ strain distributions created by a single rectangular inclusion of the FM phase (AR = 1) in the AF matrix. Inclusions with larger AR (long edge parallel to x axis) create larger strains in the matrix (see figures 4(b) and (c) for AR = 2.5 and 4, respectively). For a vertically oriented inclusion (long edge parallel to y axis) the strain distribution is the same up to the sign inversion (see figure 4(d)). Thus, an equiprobable distribution of vertically and horizontally oriented inclusions should minimize the average anisotropic strains in the sample and reduce incompatibility between the substrate and FeRh.

We further note that the largest strains are concentrated near the short edges of the inclusion and have opposite sign compared to the strain inside the inclusion. We anticipate that these strains facilitate perpendicularly oriented rectangular domain tessellations in which vertically oriented inclusions start to grow from the short edges of horizontally oriented ones (and vice versa). This conclusion is also supported by the AF/FM domain images in figures 2(a) and (b), where the presence of L-shaped interpenetrating networks is predominant at the mid-point of the transition, where AF and FM regions reach similar fractions.

To have more insight into details of the phase domain configurations, we compared $u_{xx} - u_{yy}$ strain distributions produced by a pair of identical inclusions with an AR of 2.5 in three configurations: (i) L-oriented tessellated, (ii) T-oriented tessellated, and (iii) T-oriented separated (see figures 4(e)–(g)). We found that tessellation results in penetration of strains of opposite sign into the inclusion and thus reduces the average strain inside the inclusion. On the contrary, the strain between separated inclusions increases (see figure 4(g)). The L-type configuration particularly suppresses strain near the corner apex (see the dashed circle in figure 4(e)). Hence, we deduce that zig-zag ordering of inclusions (combination of L-shapes) produces minimal anisotropic strains and is more energetically favorable. The same arguments are also applicable to the reverse transition, i.e. the growth of AF inclusions in the FM matrix, with the sign inversion of all (isotropic and anisotropic) strains.

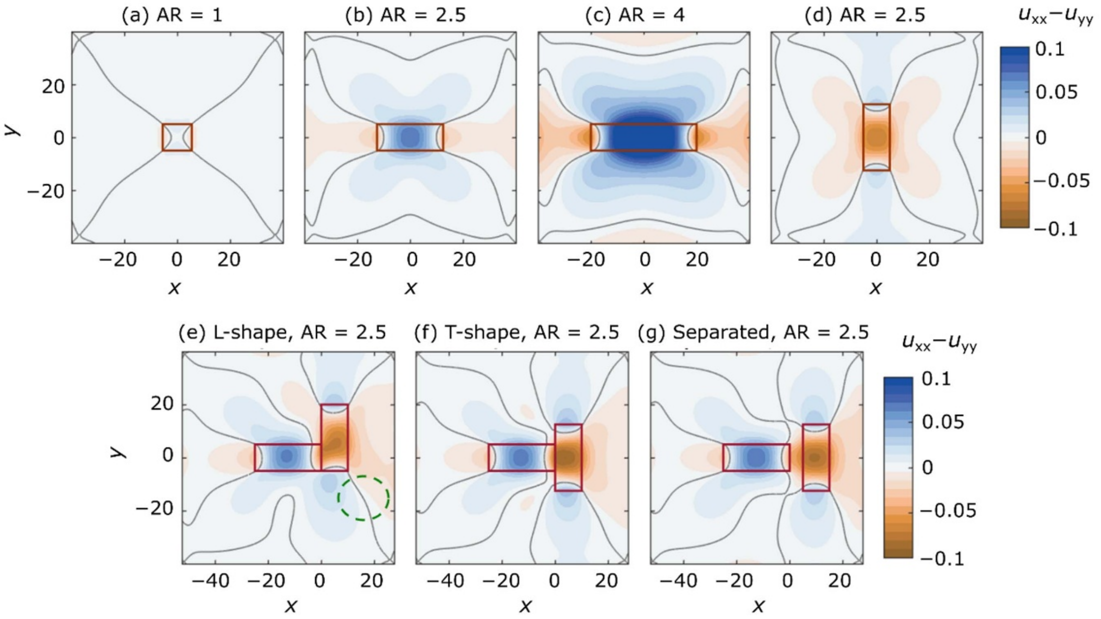

(h) Sequence during heating (i) Sequence during cooling

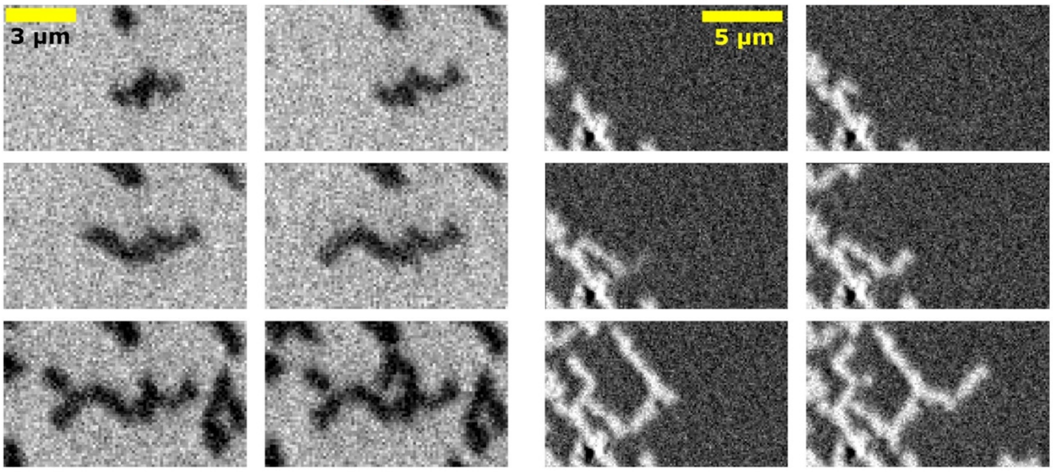

Figure 4. Link between magnetoelasticity and growth of phase domains in FeRh films. Simulations of elastic strain components $u_{xx} - u_{yy}$ for (a)–(d) an FM inclusion with indicated aspect ratios (ARs) in the AF matrix, and (e)–(g) a pair of perpendicularly oriented identical inclusions (AR = 2.5) under different arrangements. Isolines with zero $u_{xx} - u_{yy}$ strain are indicated. Sequences (shown from left to right and from top to bottom) of (h) FM domain growth during heating over a 10×6 μm^2 area, and (i) AF domain growth during cooling over a 15×9 μm^2 area. FM (AF) domains show a dark (bright) contrast.

Finer details of domain nucleation and growth can be tracked in figures 4(h) and (i), where we show zoomed in sequential optical microscopy images during heating and cooling (over reduced areas of 10×6 μm^2 and 15×9 μm^2, respectively). The images are acquired as the sample temperature is varied at 1 K min^{-1}. Individual phase domain growth events can be noticed between snapshots. We observe predominant zig-zag type growth of phase domains starting at the apex of the already existing product phase regions, confirming that an L-shape arrangement of domains is favored. However, we also see instances in which new phase regions grow as ramifications of already existing ones, following a T-type configuration (see, for instance, the last three snapshots in figure 4(h)). We conclude that while L-shape arrangements leading to zig-zag type growth of phase domains are more frequent, there is significant occurrence of T-shape arrangements that better adapt to the elastic constriction imposed by the substrate and help towards the formation of interpenetrating domain networks.

3.3. Anisotropic nucleation and growth of phase domains in a magnetic field

Optical microscopy conveniently allows imaging of the phase nucleation and growth in FeRh under applied magnetic fields, unlike PEEM microscopies [30–33], where the presence of small-to-moderate magnetic

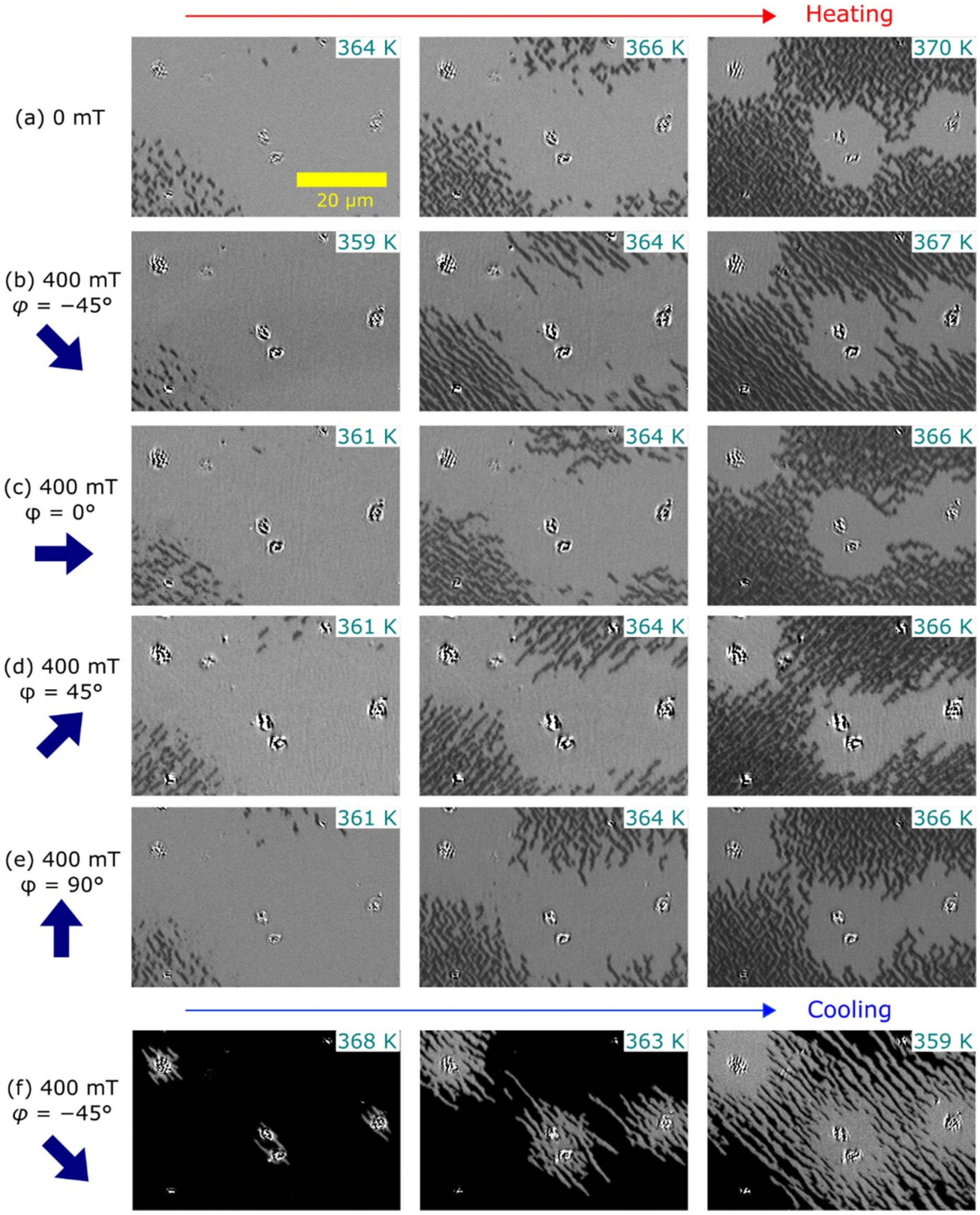

Figure 5. Magnetic field effect on the phase domain nucleation in FeRh. Optical images show the phase domain evolution over a $60 \times 40\ \mu\text{m}^2$ area during the thermally driven phase transition. Snapshots are shown for (a) heating at zero field, and for an applied field of 400 mT at an angle φ with respect to the horizontal axis: (b) $\varphi = -45^\circ$, (c) $\varphi = 0^\circ$, (d) $\varphi = 45^\circ$, (e) $\varphi = 90^\circ$. (f) Images during cooling for an applied field of 400 mT and $\varphi = -45^\circ$. The temperatures at which the images were retrieved are indicated in each inset.

fields largely disturbs image quality. To study the effect of a magnetic field applied during the thermally driven phase transition of FeRh, we used a rotatable electromagnet providing in-plane fields up to 400 mT in combination with the temperature regulation provided by a custom-made sample holder. The field direction is defined by its angle φ with respect to the horizontal axis of the images (i.e. the MgO[100] direction).

Figure 5(a) shows three snapshots of the phase domain evolution over a $60 \times 40\ \mu\text{m}^2$ area as the sample is heated across the phase transition in zero applied field. FM domain growth occurs as described before (figure 2(a)), with a degeneracy of preferred growth orientation along both diagonal directions. When repeating the heating cycle upon applying a 400 mT field at $\varphi = -45^\circ$ (figure 5(b)), the preferential growth degeneracy is broken. The growth of FM domains follows a strikingly different pattern, elongating exclusively along the diagonal matching the applied field direction, and forming much longer finger-shaped regions ($\sim$10–20 µm) in comparison with the zero-field case.

The application of a horizontal magnetic field of 400 mT ($\varphi = 0°$, figure 5(c)) does not impede the zig-zag-type growth of the product phase. However, FM domains alternate short elongations along both diagonals in order to form horizontally extended zig-zag sequences. As the phase transition progresses (see last image in figure 5(c)), AF and FM regions form rectangular networks that are similar to the zero-field case, but the symmetry breaking slightly persists in the form of horizontally elongated saw-shaped domains. We further verify that applying the magnetic field of 400 mT along the other diagonal ($\varphi = 45°$, figure 5(d)) resumes selective growth of FM domains along the applied field direction. Finally, driving the transition under a vertical magnetic field ($\varphi = 90°$, figure 5(d)) generates vertically elongated zig-zag FM domains, analogously to the horizontal field case.

The magnetic-field-induced selectivity of domain growth direction also applies to the phase transition during cooling. Figure 5(e) shows optical microscopy images of the same investigated area upon reducing the temperature under a 400 mT magnetic field applied along the diagonal direction ($\varphi = -45°$). AF domains nucleate at groove-like defects and elongate along the applied field direction forming fingers with lengths of the order of tens of microns. The regions near hole-like defects seem to quickly percolate in the AF phase. Nonetheless, a well-defined stripe domain configuration forms in the regions that are $\sim$10 µm away from the defect and are thus less susceptible to the compressive strain build-up around them.

These results suggest that the nucleation and growth characteristics of phase domains in FeRh can be selectively controlled using applied magnetic fields during the thermally driven phase transition. A sufficiently high field can break the degeneracy of preferential biaxial domain growth promoted by the substrate. However, the difference in phase domain evolution at zero field and 400 mT suggests that there must exist a magnetic field threshold needed for overcoming the elastic constriction from the substrate and providing the selective orientational growth of phase domains.

The field threshold was determined by imaging the phase-separated state over the same 60×40 µm^2 area of the sample while keeping the applied field angle at $\varphi = -45°$ and changing the strength of the applied field during each temperature-driven phase transition. Figures 6(a)–(f) exhibit optical microscopy images of the AF/FM domain coexistence during heating (temperature values not shown) under different applied fields. The FM domain growth directionality is largely present for applied field values of 400 mT (figure 6(a)), 200 mT (figure 6(b)), and 150 mT (figure 6(c)), but disappears for 50 mT and below (figures 6(d)–(f)). On the contrary, the selective phase domain growth seems to persist at lower fields in the case of cooling (figures 6(g)–(i)). The magnetic-field-induced directional growth still persists at an applied field of 50 mT (figure 6(h)), with the growth direction degeneracy being recovered at zero applied field (figure 6(i)). The insets in figure 6 show fast Fourier transform (FFT) images at each respective AF/FM domain coexistence, highlighting the crossover from uniaxial to biaxial phase domain growth as the applied field strength is reduced. At the same time, they indicate low variation of the characteristic size and spacing of the phase domains, due to the magnetoelastic considerations discussed in section 3.2.

Apparently, the field-induced selectivity of phase domain growth is present during both heating and cooling cycles. However, the magnetic field threshold for the phenomenon is different for each direction of the phase transition. During heating, the effect progressively vanishes between 150 and 50 mT, while during cooling it survives at least down to 50 mT.

3.4. Origin of magnetic-field-induced anisotropic growth of phase domains

We suggest that two mechanisms are responsible for the magnetic-field control of the phase domain growth direction in FeRh. On the one hand, magnetic dipolar interactions promote anisotropic growth by setting the magnetic moment orientation within the FM fraction at the phase-separated state. For sufficiently high fields, magnetic moments inside a FM cluster in the AF matrix will be fully aligned with the applied field. A simple stray field calculation using OOMMF [60] for a $1 \times 1 \times 0.2$ µm^3 ($l \times w \times h$) FM FeRh element with in-plane saturated moments ($M_S = 1200$ kA m^{-1}) shows that an average stray field of $\sim$0.7 T is projected within the first 50 nm adjacent to the cluster edges. Since the applied magnetic field lowers the phase transition temperature in FeRh at a rate of -8 K T^{-1} [15], the stray field effectively reduces the onset AF-to-FM transition temperature by about 5–6 K in the apex regions close to an existing FM cluster (top left panel in figure 7(a)), promoting the growth of elongated FM domains along the applied field direction.

If we consider the cooling cycle, an AF cluster is surrounded by a magnetized FM matrix. The stray field produced by FM moments penetrates the AF cluster, but at the same time, a significant reduction of the total magnetic field occurs in the FM regions adjacent to the AF cluster due to the demagnetizing field (bottom left panel in figure 7(a)). This local field reduction at the opposite FM matrix edges locally promotes the FM-to-AF phase transition, causing directional growth of AF domains during cooling.

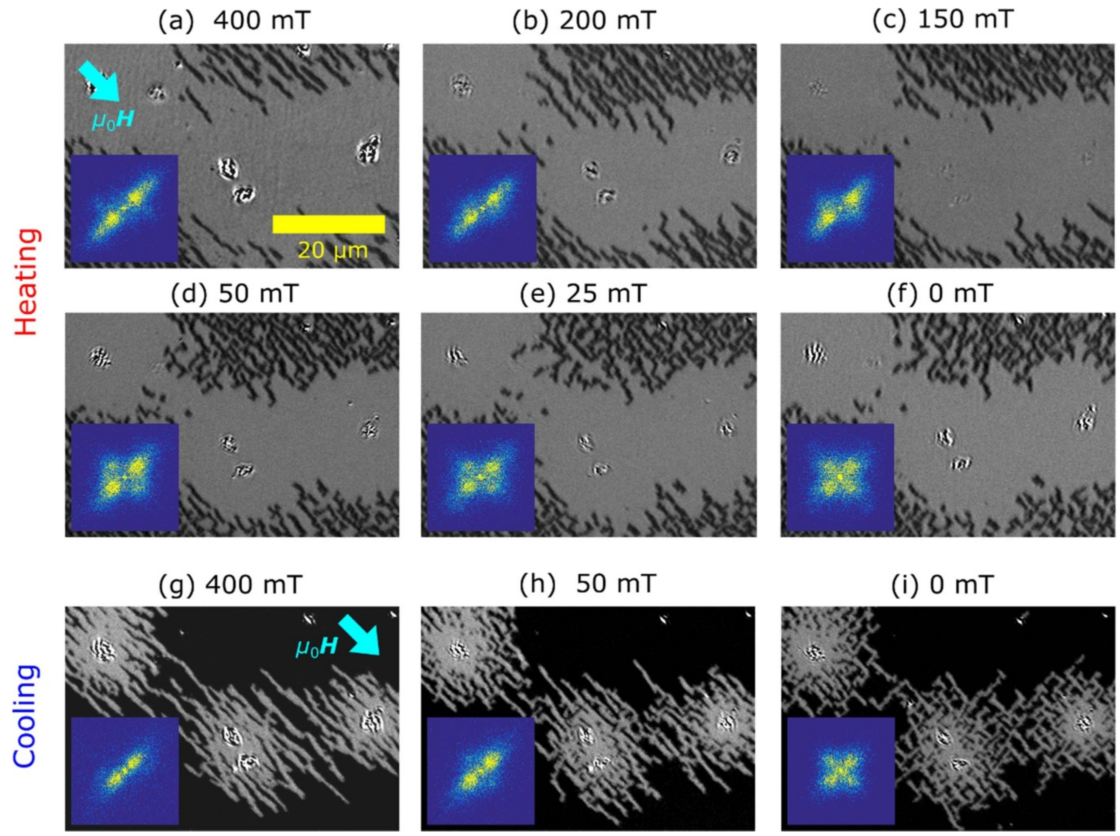

Figure 6. Magnetic field threshold for directional growth of phase domains in FeRh. (a)–(f) Optical microscopy images of the phase-separated state during heating for different values of the magnetic field applied at an angle $\varphi = -45^\circ$. (g)–(i) Images of the phase-separated state for different applied field values during cooling. The insets show two-dimensional FFT distributions calculated from the optical microscopy images near the 50:50 AF/FM phase coexistence. The magnetic field orientation for all panels is indicated by the arrows in the insets of (a) and (g).

On the other hand, we suggest that magnetostriction also promotes directional phase domain growth under an applied field, by means of the anisotropic lateral strains generated at the phase separated state. It is well known that magnetostriction has an important influence on the magnetic domain configuration due to the presence of elastic strain charges generated at domain boundaries in FM as well as AF materials [58, 59, 61]. For moderate fields up to 400 mT, we only consider effects associated with the FM phase of FeRh, which exhibits negative linear magnetostriction resulting in elastic contraction along the magnetized axis of the material [62]. While the size of anisotropic magnetostriction is considerably smaller than the isotropic lattice volume expansion at the phase transition, in the following we discuss its role in the directional phase domain growth under an applied magnetic field.

A magnetized FM cluster in the AF matrix will undergo an anisotropic $u_{xx}^{\mathrm{lin}} - u_{yy}^{\mathrm{lin}}$ elastic deformation (right top panel in figure 7(a)), promoting volume expansion and consequently the phase transition in the AF regions adjacent to the cluster edges located at the two ends of the magnetization vector (red shaded areas). Furthermore, at the remaining cluster edges, the AF FeRh matrix will be laterally compressed. This causes a slight local contraction of the unit cell and consequently increases the phase transition temperature [63], i.e. the AF phase is additionally stabilized. During cooling in an applied field, the FM matrix around an AF cluster will also undergo an anisotropic deformation (right bottom panel in figure 7(a)). Here, magnetostriction generates compressive strains within the blue shaded FM regions in the proximity of the AF cluster, locally supporting the FM-to-AF transition and enhancing the directional growth of the AF domain along the applied field direction.

Comparing the relative significance of the magnetic dipolar interactions and magnetostriction as possible mechanisms behind the observed effect, we highlight that (i) the directional growth of phase domains in the proximity of hole-like defects, where strong elastic strains are accumulated, does not seem to be disrupted; and (ii) the field threshold for oriented domain growth is not symmetric in the heating and cooling cycles, which would be expected if magnetostriction was playing a competitive role.

These factors point to magnetic dipolar interactions playing a more significant role in the field-induced anisotropic growth of phase domains. In this scenario, the observed effects would scale with the degree of FM

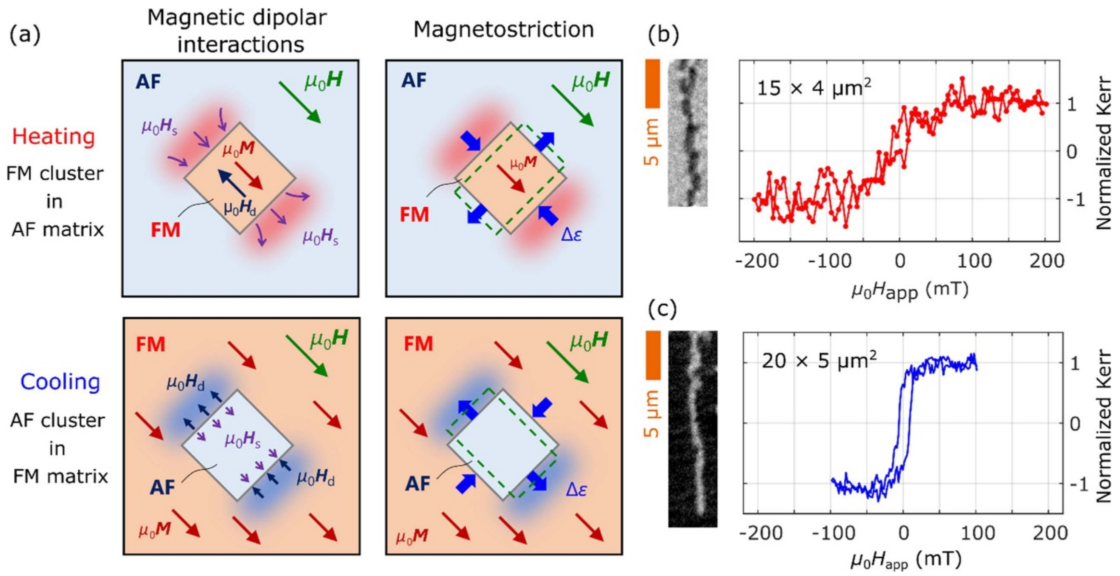

Figure 7. (a) Sketch of the mechanisms for anisotropic phase domain growth in FeRh, representing the involved magnetic fields (externally applied field $\mu_0 H$, stray field $\mu_0 H_S$, demagnetizing field $\mu_0 H_d$, magnetization flux density $\mu_0 M$) and elastic deformations (see manuscript text). The red and blue shaded regions around the FM or AF clusters represent the areas of the AF (FM) matrix where the phase transition is promoted by the application of an external magnetic field. Right panel shows magneto-optical Kerr effect hysteresis loops obtained for (b) a FM cluster in the AF matrix during the heating cycle of the phase transition, and (c) for an AF cluster in the FM matrix during the cooling cycle of the phase transition. The insets in (b), (c) show optical microscopy images of the region from where the magneto-optical signal was retrieved, where the darker (brighter) regions correspond to the FM (AF) phase. The elongated phase domains in the images are directed along the FeRh[100] direction, and the area of the images is indicated in the inset of (b), (c). The applied field for the hysteresis loop measurement was oriented perpendicular to both the FM and AF stripes , i.e. FeRh[010].

moment alignment along the applied field direction. To validate this idea, we have employed magneto-optical Kerr effect measurements to determine the strength of magnetic field needed to reorient the magnetic moments within a FM domain in the AF matrix, and within the FM matrix surrounding an AF domain.

The inset in figures 7(b) and (c) shows an optical microscopy image of an elongated FM (AF) domain in the AF (FM) matrix. These domain states were prepared by applying a 400 mT field along the FeRh[100] direction during the heating or cooling cycle. Next, the applied magnetic field was switched off while maintaining the temperature of the sample at the setting where the domain configuration had been obtained. Lastly, magneto-optical Kerr effect characterization was carried out by applying the field along the short dimension of the domains, i.e. along FeRh[010].

The resulting hysteresis loops for the two cases are shown in figures 7(b) and (c). The FM domain in the AF matrix (figure 7(b)) exhibits a hard axis loop, where magnetization is saturated along the field direction at ∼100 mT. In contrast to this, the FM region around the elongated AF domain, which can be understood as a continuous thin film with a central nonmagnetic defect, shows a loop characteristic for a softer magnetic material (figure 7(c)). Here, the magnetization switches at ∼8 mT (similar to the switching field of ∼5 mT when the whole film is in the FM phase) and fully aligns with the applied field at ∼25 mT. The magnetic field values needed to reorient the FM magnetic moments in each case agree well with the asymmetric threshold observed during heating and cooling when inducing the directional domain growth. This evidences the dominating action of the magnetic dipolar interactions and reflects that directional phase domain growth can be achieved by application of a magnetic field sufficient to orient the FM moments in the phase-separated state.

4. Conclusions

In summary, we have demonstrated that wide-field optical microscopy enables visualization of phase domain evolution across the phase transition in a 200 nm-thick epitaxial FeRh film. Domain nucleation, growth, and percolation processes are largely determined by strain from the substrate, from lateral heterogeneous strain arising from the phase coexistence, and from hole-like topographic defects. The cubic MgO substrate imposes a biaxial degeneracy in the preferred phase domain growth direction, which occurs along the principal crystal axes of FeRh. The hole-like defects create long-range (tens of microns) lateral compressive strain distributions acting as nucleation sites for the AF phase. These observations stress the importance of long-range destressing fields and the magnetoelastic coupling in defining the characteristics of phase coexistence in epitaxial FeRh films.

Furthermore, we observe that the application of a sufficiently high magnetic field causes a selective directional growth of the product phase along the field direction during both heating and cooling, breaking the preferred growth degeneracy set by the substrate. The magnetic field threshold value at which the anisotropic domain growth emerges is different for the heating and cooling cycles. We show that the main effect of the magnetic field consists in aligning the moments in the FM phase fraction, which is magnetically hard or soft during heating or cooling, respectively. While the physical origin behind the magnetic field control of phase domain patterns predominantly lies in magnetic dipolar interactions, magnetostriction effects contribute in the same direction.

Data availability statement

All data that support the findings of this study are included within the article (and any supplementary files).

Acknowledgments

We thank Laura Thevenard and Catherine Gourdon for fruitful discussions. Access to the CEITEC Nano Research Infrastructure was supported by the Ministry of Education, Youth and Sports (MEYS) of the Czech Republic under the project CzechNanoLab (LM2018110). F R was supported by a fellowship of the German Academic Exchange Service (DAAD). J H acknowledges support from the project Quality Internal Grants of BUT (KInG BUT), Reg. No. CZ.02.2.69/0.0/0.0/19_073/0016948, which is financed from the OP VVV. O G acknowledges support from Deutsche Forschungsgemeinschaft (DFG, German Research Foundation), TRR 288-422213477 (Project A09) and TRR 173-268565370 (Project B12), and also the EU FET Open RIA Grant No. 766566.

ORCID iDs

Jon Ander Arregi https://orcid.org/0000-0002-7376-2757
Jan Hajduček https://orcid.org/0000-0001-6405-5818
Olena Gomonay https://orcid.org/0000-0002-9413-0337
Vojtěch Uhlíř https://orcid.org/0000-0002-0512-6329

References

[1] Sander D *et al* 2017 The 2017 magnetism roadmap *J. Phys. D: Appl. Phys.* **50** 363001
[2] Roy S B 2013 First order magneto-structural phase transition and associated multi-functional properties in magnetic solids *J. Phys.: Condens. Matter* **25** 183201
[3] Dagotto E 2005 Complexity in strongly correlated electronic systems *Science* **309** 257–62
[4] Imry Y and Wortis M 1979 Influence of quenched impurities on first-order phase transitions *Phys. Rev.* B **19** 3580
[5] Kalinin S V and Spaldin N A 2013 Functional ion defects in transition metal oxides *Science* **341** 858–9
[6] Bucsek A N, Nunn W, Jalan B and James R D 2020 Energy conversion by phase transformation in the small-temperature-difference regime *Annu. Rev. Mater. Res.* **50** 283–318
[7] Campanini M *et al* 2018 Magnetic shape memory turns to nano: microstructure controlled actuation of free-standing nanodisks *Small* **14** 1803027
[8] Zhao Y D, Kang J F and Ielmini D 2021 Materials challenges and opportunities for brain-inspired computing *MRS Bull.* **46** 978–86
[9] Fallot M and Hocart R 1939 Sur l'apparition du ferromagnétisme par élévation de température dans des alliages de fer et de rhodium *Rev. Sci.* **77** 498–500
[10] Lewis L H, Marrows C H and Langridge S 2016 Coupled magnetic, structural and electronic phase transitions in FeRh *J. Phys. D: Appl. Phys.* **49** 323002
[11] Arregi J A, Caha O and Uhlíř V 2020 Evolution of strain across the magnetostructural phase transition in epitaxial FeRh films on different substrates *Phys. Rev.* B **101** 174413
[12] Kouvel J S and Hartelius C 1962 Anomalous magnetic moments and transformations in the ordered alloy FeRh *J. Appl. Phys.* **33** 1343–4
[13] Uhlíř V, Arregi J A and Fullerton E E 2016 Colossal magnetic phase transition asymmetry in mesoscale FeRh stripes *Nat. Commun.* **7** 13113
[14] Temple R C, Rosamond M C, Massey J R, Almeida T P, Linfield E H, McGrouther D, McVitie S, Moore T A and Marrows C H 2021 Phase domain boundary motion and memristance in gradient-doped FeRh nanopillars induced by spin injection *Appl. Phys. Lett.* **118** 122403
[15] Maat S, Thiele J-U and Fullerton E 2005 Temperature and field hysteresis of the antiferromagnetic-to-ferromagnetic phase transition in epitaxial FeRh films *Phys. Rev.* B **72** 214432
[16] Kouvel J S 1966 Unusual nature of the abrupt magnetic transition in FeRh and its pseudobinary variants *J. Appl. Phys.* **37** 1257–8
[17] Annaorazov M P, Nikitin S A, Tyurin A L, Asatryan K A and Dovletov A K 1996 Anomalously high entropy change in FeRh alloy *J. Appl. Phys.* **79** 1689–95
[18] Pecharsky V K and Gschneidner Jr J K A 1999 Magnetocaloric effect and magnetic refrigeration *J. Magn. Magn. Mater.* **200** 44–56

[19] Lyubina J 2017 Magnetocaloric materials for energy efficient cooling *J. Phys. D: Appl. Phys.* **50** 053002

[20] Belo J H, Pires A L, Araújo J P and Pereira A M 2019 Magnetocaloric materials: from micro-to nanoscale *J. Mater. Res.* **34** 134–57

[21] Nikitin S A, Myalikgulyev G, Tishin A M, Annaorazov M P, Asatryan K A and Tyurin A L 1990 The magnetocaloric effect in $Fe_{49}Rh_{51}$ compound *Phys. Lett.* A **148** 363–6

[22] Chirkova A, Skokov K P, Schultz L, Baranov N V, Gutfleisch O and Woodcock T G 2016 Giant adiabatic temperature change in FeRh alloys evidenced by direct measurements under cyclic conditions *Acta Mater.* **106** 15–21

[23] Cherifi R O *et al* 2014 Electric-field control of magnetic order above room temperature *Nat. Mater.* **13** 345–51

[24] Liu Z Q *et al* 2016 Full electroresistance modulation in a mixed-phase metallic alloy *Phys. Rev. Lett.* **116** 097203

[25] Fina I, Quintana A, Martí X, Sánchez F, Foerster M, Aballe L, Sort J and Fontcuberta J 2018 Reversible and magnetically unassisted voltage-driven switching of magnetization in FeRh/PMN-PT *Appl. Phys. Lett.* **113** 152901

[26] Qiao K *et al* 2020 Regulation of phase transition and magnetocaloric effect by ferroelectric domains in FeRh/PMN-PT heterojunctions *Acta Mater.* **191** 51–59

[27] Binder K 1987 Theory of first-order phase transitions *Rep. Prog. Phys.* **50** 783–859

[28] Yokoyama Y, Usukura M, Yuasa S, Suzuki Y, Miyajima H and Katayama T 1998 MFM observation of magnetic phase transitions in ordered FeRh systems *J. Magn. Magn. Mater.* **177** 181–2

[29] Manekar M, Mukherjee C and Roy S B 2007 *Europhys. Lett.* **80** 17004

[30] Baldasseroni C, Bordel C, Gray A X, Kaiser A M, Kronast F, Herrero-Albillos J, Schneider C M, Fadley C S and Hellman F 2012 Temperature-driven nucleation of ferromagnetic domains in FeRh thin films *Appl. Phys. Lett.* **100** 262401

[31] Mariager S O, Le Guyader L, Buzzi M, Ingold G and Quitmann C 2013 Imaging the antiferromagnetic to ferromagnetic first order phase transition of FeRh (arXiv:1301.4164)

[32] Temple R C *et al* 2018 Antiferromagnetic-ferromagnetic phase domain development in nanopatterned FeRh islands *Phys. Rev. Mater.* **2** 104406

[33] Baldasseroni C, Bordel C, Antonakos C, Scholl A, Stone K H, Kortright J B and Hellman F 2015 Temperature-driven growth of antiferromagnetic domains in thin-film FeRh *J. Phys.: Condens. Matter* **27** 256001

[34] Keavney D J, Choi Y, Holt M V, Uhlíř V, Arena D, Fullerton E, Ryan P J and Kim J-W 2018 Phase coexistence and kinetic arrest in the magnetostructural transition of the ordered alloy FeRh *Sci. Rep.* **8** 1778

[35] Ahn Y *et al* 2022 X-ray nanodiffraction imaging reveals distinct nanoscopic dynamics of an ultrafast phase transition *Proc. Natl Acad. Sci. USA* **119** e2118597119

[36] Zhou X, Matthes F, Bürgler D E and Schneider C M 2016 Magnetic surface domain imaging of uncapped epitaxial FeRh (001) thin films across the temperature-induced metamagnetic transition *AIP Adv.* **6** 015211

[37] Gatel C, Warot-Fonrose B, Biziere N, Rodríguez L A, Reyes D, Cours R, Castiella M and Casanove M J 2017 Inhomogeneous spatial distribution of the magnetic transition in an iron-rhodium thin film *Nat. Commun.* **8** 15703

[38] Almeida T P, McGrouther D, Temple R, Massey J, Li Y, Moore T, Marrows C H and McVitie S 2020 Direct visualization of the magnetostructural phase transition in nanoscale FeRh thin films using differential phase contrast imaging *Phys. Rev. Mater.* **4** 034410

[39] Nava Antonio G, Bertelli I, Simon B G, Medapalli R, Afanasiev D and van der Sar T 2021 Magnetic imaging and statistical analysis of the metamagnetic phase transition of FeRh with electron spins in diamond *J. Appl. Phys.* **129** 223904

[40] Fisher B 1976 Metal-semiconductor domain configurations during switching of VO_2 single crystals *J. Phys. C: Solid State Phys.* **9** 1201–9

[41] Lai Y W, Scheerbaum N, Hinz D, Gutfleisch O, Schäfer R, Schultz L and McCord J 2007 Absence of magnetic domain wall motion during magnetic field induced twin boundary motion in bulk magnetic shape memory alloys *Appl. Phys. Lett.* **90** 192504

[42] Lai Y W, Schäfer R, Schultz L and McCord J 2008 Direct observation of AC field- induced twin-boundary dynamics in bulk NiMnGa *Acta Mater.* **56** 5130–7

[43] Takhsha Ghahfarokhi M, Arregi J A, Casoli F, Horký M, Cabassi R, Uhlíř V and Albertini F 2021 Microfabricated ferromagnetic-shape-memory Heuslers: the geometry and size effects *Appl. Mater. Today* **23** 101058

[44] Del Valle J *et al* 2021 Spatiotemporal characterization of the field-induced insulator-to-metal transition *Science* **373** 907–11

[45] Saidl V *et al* 2016 Investigation of magneto-structural transition in FeRh by reflectivity and transmittance measurements in visible and near-infrared spectral region *New J. Phys.* **18** 083017

[46] Cress C D *et al* 2020 Direct-write of nanoscale domains with tunable metamagnetic order in FeRh thin films *ACS Appl. Mater. Interfaces* **13** 836–47

[47] Taaev T A, Amirov A A, Aliev A M, Chirkova A, Soldatov I V and Schäfer R 2022 Kerr microscopy study of magnetic phase transition in $Fe_{49}Rh_{51}$ *Phys. Met. Metallogr.* **123** 402–6

[48] Nečas D and Klapetek P 2012 Gwyddion: an open-source software for SPM data analysis *Cent. Eur. J. Phys.* **10** 181–8

[49] Takahashi M and Oshima R 1995 Stress induced phase transition of iron-rhodium alloys *J. Phys. IV France* **5** C8-491–C8-496

[50] Castiella M, Gatel C, Bobo J F, Ratel-Ramond N, Tan R, Respaud M and Casanove M J 2015 Structural investigation of magnetic FeRh epitaxial films *Mater. Res. Express* **2** 086401

[51] Chen X Z *et al* 2017 Tunneling anisotropic magnetoresistance driven by magnetic phase transition *Nat. Commun.* **8** 449

[52] de Vries M A, Loving M, McLaren M, Brydson R M D, Liu X, Langridge S, Lewis L H and Marrows C H 2014 Asymmetric "melting" and "freezing" kinetics of the magnetostructural phase transition in B2-ordered FeRh epilayers *Appl. Phys. Lett.* **104** 232407

[53] Motyčková L, Arregi J A, Staňo M, Průša S, Částková K and Uhlíř V 2023 Preserving metamagnetism in self-assembled FeRh nanomagnets *ACS Appl. Mater. Interfaces* **15** 8653–65

[54] Thompson C V 2012 Solid-state dewetting of thin films *Annu. Rev. Mater. Res.* **42** 399–434

[55] Arregi J A, Horký M, Fabianová K, Tolley R, Fullerton E E and Uhlíř V 2018 Magnetization reversal and confinement effects across the metamagnetic phase transition in mesoscale FeRh structures *J. Phys. D: Appl. Phys.* **51** 105001

[56] Kwak B S, Erbil A, Wilkens B J, Budai J D, Chisholm M F and Boatner L A 1992 Strain relaxation by domain formation in epitaxial ferroelectric thin films *Phys. Rev. Lett.* **68** 3733

[57] Meer H, Schreiber F, Schmitt C, Ramos R, Saitoh E, Gomonay O, Sinova J, Baldrati L and Kläui M 2020 Direct imaging of current-induced antiferromagnetic switching revealing a pure thermomagnetoelastic switching mechanism in NiO *Nano Lett.* **21** 114–9

[58] Meer H *et al* 2022 Strain-induced shape anisotropy in antiferromagnetic structures *Phys. Rev.* B **106** 094430

[59] Wittman A *et al* 2022 Role of substrate clamping on anisotropy and domain structure in the canted antiferromagnet α-Fe_2O_3 *Phys. Rev.* B **106** 224419

[60] Donahue M J and Porter D G 1999 OOMMF user's guide, version 1.0 *Interagency Report NIST IR 6376* (Gaithersburg, MD) (available at: http://math.nist.gov/oommf)

[61] Gomonay H and Loktev V M 2002 Magnetostriction and magnetoelastic domains in antiferromagnets *J. Phys.: Condens. Matter* **14** 3959

[62] Ricodeau J A and Melville D 1974 High field magnetostriction in a meta-magnetic FeRh alloy *J. Phys. France* **35** 149–52

[63] Komlev A S, Karpenkov D Y, Kiselev D A, Ilina T S, Chirkova A, Gimaev R R, Usami T, Taniyama T, Zverev V I and Perov N S 2021 Ferromagnetic phase nucleation and its growth evolution in FeRh thin films *J. Alloys Compd.* **874** 159924